The SARS-CoV-2 nucleocapsid protein interferes with the full enzymatic activation of UPF1 and its interaction with UPF2

Veronica Nuccetelli, Makram Mghezzi-Habellah, Séverine Deymier, Armelle Roisin, Francine Gérard-Baraggia, Cecilia Rocchi, Pierre-Damien Coureux, Patrice Gouet, Andrea Cimarelli, Vincent Mocquet, et al.

Nucleic Acids Research, 2025, gkaf010
https://doi.org/10.1093/nar/gkaf010
Nucleic Acid Enzymes

The SARS-CoV-2 nucleocapsid protein interferes with the full enzymatic activation of UPF1 and its interaction with UPF2

Veronica Nuccetelli[1,2,†], Makram Mghezzi-Habellah[3,†], Séverine Deymier[4], Armelle Roisin[3], Francine Gérard-Baraggia[1], Cecilia Rocchi[1,5], Pierre-Damien Coureux[1], Patrice Gouet[1], Andrea Cimarelli[4], Vincent Mocquet[3] and Francesca Fiorini[1,*]

[1]Molecular Microbiology and Structural Biochemistry, MMSB-IBCP, CNRS UMR 5086 , Université Claude Bernard Lyon 1, F-69367 Lyon, France
[2]Department of Drug Chemistry and Technologies, Sapienza University of Rome, I-00185 Rome, Italy
[3]Laboratoire de Biologie et Modélisation de la Cellule, Ecole Normale Supérieure de Lyon, CNRS UMR 5239, Inserm U1293, Université Claude Bernard Lyon 1, F-69364 Lyon, France
[4]Centre International de Recherche en Infectiologie (CIRI), Ecole Normale Supérieure de Lyon, Université Claude Bernard Lyon 1, Inserm, U1111, CNRS, UMR5308, F-69364 Lyon, France
[5]Division of Structural Biology - Nuffield Department of Medicine, University of Oxford, OX3 7BN Oxford, England

[*]To whom correspondence should be addressed. Tel: +33 4 72 72 26 31; Fax: +33 4 72 72 26 01; Email: francesca.fiorini@ibcp.fr
[†]These authors contributed equally.

Abstract

The nonsense-mediated mRNA decay (NMD) pathway triggers the degradation of defective mRNAs and governs the expression of mRNAs with specific characteristics. Current understanding indicates that NMD is often significantly suppressed during viral infections to protect the viral genome. In numerous viruses, this inhibition is achieved through direct or indirect interference with the RNA helicase UPF1, thereby promoting viral replication and enhancing pathogenesis. In this study, we employed biochemical, biophysical assays and cellular investigations to explore the interplay between UPF1 and the nucleocapsid (Np) protein of SARS-CoV-2. We evaluated their direct interaction and its impact on inhibiting cellular NMD. Furthermore, we characterized how this interaction affects UPF1's enzymatic function. Our findings demonstrate that Np inhibits the unwinding activity of UPF1 by physically obstructing its access to structured nucleic acid substrates. Additionally, we showed that Np binds directly to UPF2, disrupting the formation of the UPF1/UPF2 complex essential for NMD progression. Intriguingly, our research also uncovered a surprising pro-viral role of UPF1 and an antiviral function of UPF2. These results unveil a novel, multi-faceted mechanism by which SARS-CoV-2 evades the host's defenses and manipulates cellular components. This underscores the potential therapeutic strategy of targeting Np-UPF1/UPF2 interactions to treat COVID-19.

Graphical abstract

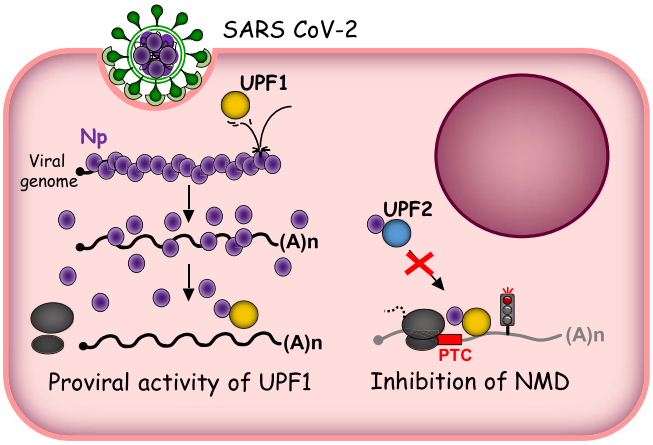

Received: July 17, 2024. **Revised:** January 1, 2025. **Editorial Decision:** January 2, 2025. **Accepted:** January 6, 2025

Introduction

Nonsense-mediated mRNA decay (NMD) was originally described as a eukaryotic translation-dependent quality control mechanism that degrades mRNAs harboring premature translation termination codons (PTC (1–3)). NMD exerts a broader global influence by regulating the stability of numerous error-free transcripts, thereby influencing 5–20% of cellular gene expression (4). Beyond the PTC, all the NMD-prone transcripts possess unique characteristics, such as the long 3′ untranslated regions (UTRs), exon junction complexes in the 3′UTR or a short open reading frames in the 5′UTR (uORFs), which make them susceptible to NMD (5). Recent studies have unveiled the role of NMD as a restrictor of RNA virus replication (reviewed in (6–8). This phenomenon is likely attributed to the replication strategy of RNA- and retro-viruses, which undergo selective pressure to maximize the coding capacity of their viral RNA without increasing the size of their genome. As a result, certain features, such as internal termination codons (iTC) due to multiple ORFs and long 3′ UTRs, are introduced into viral RNAs and make them prone to NMD. The list of phyto- and mammalian viruses sensitive to NMD restriction continues to expand, encompassing numerous families (9–27). These viruses have evolved by developing strategies to counteract NMD and sometimes co-opting the NMD factors for their advantage. They employ either RNA structures that directly *cis*-protects the viral genome (10,11,28–30) or *trans*-acting factors that target various NMD proteins (9,14–21,24–26).

The RNA helicase UPF1 (UP-frameshift 1) is the central factor of NMD. This multifunctional enzyme comprises a conserved helicase core domain that, powered by adenosine triphosphate (ATP) hydrolysis, is capable of unwinding double-stranded nucleic acids (NAs) in a 5′ to 3′ direction. UPF1 is a dynamic nucleoprotein complexe remodeler. It moves along single-stranded NAs, displacing the proteins that are tightly attached to the substrate. The activity of UPF1 is inhibited by two domains that surround the helicase core: the N-terminal CH domain, which is rich in cysteine and histidine residues, and the C-terminal SQ domain, which contains clusters of serine-glutamine residues. To date, the only enzymatic activation of UPF1 that has been characterized during NMD is that exerted by UPF2. Indeed, the binding of UPF2 to the CH domain allows for its displacement, inducing the activation of UPF1 by shifting the enzyme from an RNA-clamping to a relaxed-translocating mode. Few viral factors have been described to integrate this complex enzymatic regulation and affect NMD. For example, the Tax protein of human T-lymphotropic virus 1 retrovirus (HTLV-1) directly binds to both UPF1 and UPF2 (12). Tax, by interacting with the helicase core domain of UPF1, induces a loss of affinity for the substrate resulting in blocking of ATPase and translocation activities (20). It has also been reported that HTLV-1 Rex inhibits NMD via interaction with UPF1; however, molecular details are not yet available (26,31). An interesting case is represented by human immunodeficiency virus-1 (HIV-1) that not only evades NMD but also usurps UPF1 to promote viral replication (15,32,33). In this context, UPF1 has a pro-viral effect by contributing to enhancing the viral RNA stability and translation and the assembly of new virions (15,32–34). This pro-viral function of UPF1 is independent of UPF2, which is excluded from UPF1-containing viral RNPs. UPF2 has a genuine antiviral activity by inhibiting HIV-1 replication by promoting viral RNA decay (15,34).

RNA viruses of the Flaviviridae family also disrupt NMD through various mechanisms (18,21,22). Among them, Zika virus (ZIKV) directly targets UPF1 via its capsid (CA): the protein that interacts with and packages viral RNA (Fontaine 2018). This interaction occurs in both the nucleus and cytoplasm and appears to lead to the specific proteasomal degradation of nuclear UPF1 (18). The implications of this nuclear interaction for NMD and the effect of ZIKV CA on the activity of cytoplasmic UPF1 need further clarification.

The interplay between NMD and the Mouse Hepatitis Virus (MHV), a prototypic member of the Betacoronavirus gender to which belong Severe Acute Respiratory Syndrome (SARS) and Middle East Respiratory Syndrome viruses, is well described (19). In this study, the authors showed that MHV genomic and some sub-genomic RNAs are NMD targets. Indeed, depletion of NMD factors, such as UPF1 and UPF2, promotes the accumulation of viral RNAs early in infection, leading to the production of higher titers of MHV and enhanced replication (17). The MHV factor that antagonizes NMD is the nucleocapsid protein (Np), a viral structural protein that binds to and organizes the viral genome within virions (19,35). Consistently with this results, two proteomic studies identified UPF1 as a potential molecular partner of Np in Infectious Bronchitis Virus Coronavirus and SARS-CoV-2 (36,37). Notably, UPF1 has also been shown to directly and specifically bind to SARS-CoV-2 genomic and sub-genomic RNAs in infected human cells by two research groups (38,39). However, the direct interaction between CoV Np and UPF has not yet been confirmed, and mechanistic insights into NMD inhibition are also unknown.

In this study, we used biochemical and biophysical assays combined with cellular studies to understand whether and how SARS-CoV-2 manages the NMD pathway. We elucidated the molecular mechanism through which the SARS-CoV-2 Np protein impacts the activity of UPF1, resulting in the stabilization of NMD-sensitive reporter transcripts. Np exerts a dual-control mechanism on UPF1 by inhibiting both its activity and its activation and hijacking it for its advantage. Our study provides valuable molecular and cellular insights into this intricate inhibitory mechanism and underscores the significance of NMD in restricting SARS-CoV-2.

Materials and methods

Cell culture

Vero E6, HEK 293T and HeLa cells were cultured in DMEM (invitrogen) complemented with 5% FCS and penicillin/streptomycin at 37°C, 5% CO_2.

NMD assay

NMD assays were performed as described previously (20): 0.5 μg of a β-globin reporter minigene either with a WT sequence (Gl-WT) or with a PTC in the second exon (Gl-PTC) was transfected in 0.25×10^6 HeLa or Vero E6 cells with jetprime reagent (polyplus transfection). When indicated, 0.5 μg of the SARS-CoV-2 Np coding plasmid (Addgene, cat.141391) was co-transfected as well. For VeroE6 cells, we used 1 μg of the SARS-CoV-2 Np coding plasmid. Forty-eight hours after tranfection, cells were harvested and total mRNAs were extracted using the Macherey–Nagel RNA easy extraction kit. Globin mRNA was quantified by reverse transcription–polymerase chain reaction (RT-qPCR) using

the QuantiTect SYBR Green qRTPCR kit (Qiagen) and the following primers (5-TTGGGGATCTGTCCACTCC-3, 5-CACACCAGCCACCACTTTC-3). Normalization was carried out with respect to Renilla mRNA (primers: 5_-CTAACCTCGCCCTTCTCCTT-3, 5_-TCGTCCATGCTGAGAGTGTC-3) expressed from a co-transfected Renilla luciferase plasmid (0.5 μg) and NMD insensitive. The mean of the Globin/Renilla ratio ($n \geq 3$) was plotted in the graph and the error bars correspond to the SD. In the case of UPF1 extinction experiments, 10 nM of siRNA duplexes (either control (MISSION siRNA universal negative control, SIGMA Cat. SIC002-1NMOL) or targeting UPF1 (5-GAUGCAGUUCCGCUCCAUU-3) were transfected 1 day before plasmid transfection, following the manufacturer recommendations. In the experiments evaluating Globin PTC mRNA decay, transcription was inhibited with 20 μM of Triptolide for 0, 1 or 2 h before cells harvest. After RNA extraction and qRT-PCR, the globin/Renilla ratio was calculated. Then, each time point was normalized to $t = 0$h. Finally, the logarithmic function was calculated for each coordinate as f(x)=ln(t(x)/t0) to obtain a linear regression of decay (y=-ax). Half-lives were calculated for each replicate, when indicated (with t1/2=(ln2)/a) *P* values were calculated by performing a Student's t-test (unpaired, two-tailed).

Viral replication

We used a replicative SARS-CoV-2 (Wuhan strain) bearing the mNeongreen reporter replacing the ORF7, kindly obtained from Pei-Yong Shi at the University of Texas Medical Branch, Galveston, TX, USA (40). SARS-CoV-2 mNeonGreen viral stocks were produced in Vero E6 cells. When indicated, Vero E6 cells were transfected with 4 μg of DNAs coding for HA-UPF1, HA-UPF2 or a pCMV empty as a negative control or with Globin and Renilla coding plasmids with jet prime reagent. Cells were challenged 18 h later with SARS-CoV-2 mNeonGreen at multiplicities of infection (MOIs) of 0.1, and the extent of viral replication was determined 18 h post-infection by flow cytometry on a MacsQuant cytometer. The results were normalized to the control condition corresponding to infected cells transfected with pCMV empty vector.

Protein expression and purification

Human UPF1-HD (295–914 aa), UPF1-CH-HD (115–914 aa) and UPF2 (704–1204) proteins were expressed and purified as described in (41,42). SARS-CoV-2 Np protein fragments (Np-L (50–370aa), Np-NTD (50–138 aa), Np-CTD (250–370 aa) and Np-NTD-SRD (50–250 aa)) were cloned in pET52b + in frame with a C-terminal 10xHistidine tag by standard molecular biology techniques. Recombinant proteins were produced from *Escherichia coli* BL21(DE3) Rosetta bacteria (Sigma Aldrich, cat. 71 403). Bacterial cells were grown in an Luria Broth (LB) medium for 16 h at 25°C, and protein expression was induced with 0.1 mM IPTG (isopropyl-β-dthiogalactopyranoside, Sigma Aldrich, cat. PHG000110). Cultures were incubated for 6 h at 18°C under continuous shaking, then harvested by centrifugation for 15 min at 5000 g. Each pellet was resuspended with buffer A (50 mM Tris-HCl pH 7.5, 150 mM NaCl, 20 mM imidazole, 5 mM β-mercaptoethanol, 0.5 mM CaCl2 and 20% glycerol, v/v) supplemented with 1 mM of adenosine triphosphate (ATP, Jena Bioscience cat. NU-1010), 1 mM MgCl2, DNase I (New England Biolabs, Cat. M0303S), RNaseA (Sigma Aldrich Cat. RNASEA-RO) and Protease Inhibitor Cocktail tablet (ROCHE, cOmplete™ Sigma Aldrich cat. 11 836 170 001). After 2 h of incubation at 4°C, the soluble lysate was applied to a prepacked nickel column (HisTrap HP column, Cytiva Europe GmbH, France cat. GE17-5247-01) and fractionated on an AKTA pure system (Cytiva Europe GmbH, France) using a linear gradient from buffer A to buffer B (buffer A supplemented with 0.5 M imidazole) over 10 column volumes. A second step of purification was carried out using a Heparin affinity column (HiTrap Heparin HP Cytiva Europe GmbH, France cat. 17 040 703). The proteins were eluted using a buffer containing 50 mM Tris-HCl pH 7.5, 2 M NaCl, 1mM DL-Dithiothréitol (DTT), 0.1%, IGEPAL® CA-630 and 20% (v/v) glycerol.

Microscale thermophoresis

Microscale thermophoresis (MST) utilizes an infrared laser to induce a precise temperature change in a sample, enabling the characterization and quantification of binding events through the monitoring of fluorescence changes. For this experiment, UPF1-HD, UPF1-CH-HD and UPF2 (770–1204) were labeled with the RED-tris-NTA 2nd Generation dye using the Monolith His-Tag Labeling Kit in accordance with the manufacturer's instructions (Nano Temper Technologies, cat. MO-L018). Binding experiments were carried out using 200 nM of labeled protein and serial dilution of unlabeled ligand (as indicated in figures) in a phosphate-based buffer as advised by the manufacture instructions. Samples were loaded into a premium-coated capillaries (NanoTemper, cat. MO-K02) and analyzed with NanoTemper Monolith NT.115 instrument set at 30°C with an excitation power of 60%. After data acquisition, the fluorescence traces were analyzed using software provided by the manufacturer. Binding curves are generated by plotting normalized fluorescence signals against the concentration of the binding partner. The binding affinity (Kd) and stoichiometry of the interaction were determined by fitting the data to appropriate binding models.

Protein co-precipitation

Immunoprecipitations were carried out in 1.3×10^6 HEK 293T cells transfected with the indicated combinations of SARS-CoV-2 Np coding plasmid (2 μg- addgene cat.141391), Myc-UPF1 (2 μg) and HA-UPF2 (5 μg). Forty-eight hours after transfection, cells were washed two times with PBS and lysed with 1 ml of lysis buffer (50 mM Tris–Cl, pH 8, 1% NP40, 0.5% sodium deoxycholate, 0.05% SDS, 0.1 mM EDTA, 150 mM NaCl, protease inhibitor (Roche)) and with 0.1 mg/ml of RNAseA (Promega), when indicated, for 15 min at 4°C. Half of the soluble fraction was incubated with 2 μg of the indicated antibody (mouse anti-HA) (Clone 7, Millipore), anti-Myc (05–419, Millipore) and rabbit anti-UPF1 (A301-902A, bethyl) overnight at 4°C. Mixed protein A and protein G magnetic beads (10 μl- dynabeads, Invitrogene) were coated with 0.3% BSA in PBS 1X and further added to the cell lysates for 3 h and 30 min before three extensive washings in lysis buffer. Finally, beads were resuspended in laemlli buffer with loading dye to run western blots, as indicated.

The steady state calmodulin-binding peptide (CBP) pull-down procedure was conducted following the method outlined by (41,42). About 2 μg of bait protein were combined with about 10 times the amount of prey protein in a binding buffer consisting of 20 mM Tris-HCl pH 7.5, 150 mM NaCl,

1 mM DTT, 1 mM MgCl2, 2mM CaCl2 and 10% (v/v) glycerol, then incubated for 30 min at 37°C prior to resin mixing. For dose-dependent CBP pulldown, we mixed about 2 μg of CBP-UPF1-CH-HD with about 4 μg of UPF2 (770–1204) or Np and about 4, 6 and 8 μg of Np or UPF2 (770–1204) before incubation. Unbound proteins were removed by washing with binding buffer containing 200 mM NaCl. The proteins bound to the affinity beads were eluted using a buffer containing 20 mM EGTA, with the tubes shaken for 30 min at 30°C at 1400 rpm in a thermomixer. Eluates were separated by 12% sodiumdodecyl sulphate-polyacrylamide gel electrophoresis (SDS-PAGE) and visualized through Coomassie staining.

ATP hydrolysis

The steady-state experiments ATPase assays were carried out as described in (41). Before initiating the ATP assay, solutions containing either 5 μM of UPF1-HD or 5 μM UPF1-HD combined with 50 μM of Np, or 50 μM of Np alone, were incubated for 30 min at 37°C. Subsequently, 1 μl of each sample was incubated at 30°C in a 10-μl reaction mixture consisting of 20 mM MES pH 6.5, 100 mM potassium acetate, 1 mM DTT, 0.1 mM EDTA, 1 mM magnesium acetate, 1 mM zinc sulfate, 5% (v/v) glycerol, 2 μCi of [γ32P]-ATP (800 Ci/mmol, Revvity), 25 μM cold ATP and 50 μM of polyU. At specified intervals, 2 μl reaction aliquots were withdrawn and quenched with 10 mM EDTA and 0.5% (v/v) SDS. Samples were then analyzed by phosphorimaging following thin-layer chromatography on polyethyleneimine cellulose plates (Merck) using 0.35 M potassium phosphate (pH 7.5) as the migration buffer.

In vitro helicase assay

The 5′ single-strand overhang or blunt DNA duplexes were constructed using oligonucleotides as detailed in Supplementary Figure S2A. Initially, 50 pmol of radiolabeled FF2 was combined with 60 pmol of either FF1 or FF3 oligonucleotides in 100 μl of F100 buffer (20 mM MES pH 6.0, 100 mM potassium acetate, 1 mM DTT, 0.1 mM EDTA). The mixtures were heated to 95°C for 3 min and then gradually cooled to 20°C. Subsequently, DNA duplexes were purified on a native 6% (w/v) polyacrylamide gel (29:1) in 1x TBE buffer at 4°C. Single-run helicase assay was performed premixing the radiolabelled substrate (25 nM, final concentration) was mixed with an excess of UPF1, Np or preformed complexes (1 μM of UPF1 and 2 μM of Np) in F100 helicase buffer and incubated for 5 min at 30°C. The reaction was initiated by adding a mixture containing ATP and MgCl2 (1 mM, final concentrations), an excess of cold DNA strand (0.3 μM; to trap released DNA strands) and heparin (1 mg/ml; to trap free/released UPF1 and Np molecules). Reaction aliquots were withdrawn at various times, quenched with 150 mM sodium acetate, 10 mM EDTA, 0.5% (w/v) SDS, 25% (w/v) Ficoll-400, 0.05% (w/v) xylene cyanol, 0.05% (w/v) and bromophenol blue, and analyzed by polyacrylamide gel electrophoresis and phosphorimaging on a Typhoon-Trio (GE Healthcare), as described in (42).

Streptavidin displacement assay

The streptavidin displacement assay was conducted following the protocol outlined in (43). Using the helicase domain of UPF1, Np truncations or preformed protein complexes as specified, a radiolabelled 3′-biotinylated 30-mer DNA substrate (Supplementary Figure S2A, from Sigma Aldrich) was bound to a Streptavidin monomer (Promega, cat. Z7041) in an F100 buffer.

For the displacement assay, 50 nM of DNA substrate was preincubated for 5 min at 30°C with 4 μM of UPF1-HD, 8 μM Np, or preformed protein complexes in an F100 buffer. The enzymatic reaction was initiated by adding 2 mM ATP together with 4 μM of free biotin. At defined incubation times, 2 μl of reaction aliquots were mixed with 5 μl of quench buffer (150 mM NaAc, 10 mM EDTA, 0.5% (w/v) SDS, 25% (w/v) Ficoll-400, 0.05% (w/v) xylene cyanole, 0.05% (w/v) bromophenol blue) in preset tubes and immediately loaded onto the running gel. Samples were separated by an 8% (w/v) polyacrylamide gel containing 0.3% SDS and detected using a Typhoon 9400 phosphorimaging system and ImageQuant software (GE Healthcare).

Electrophoretic mobility shift assay

The oligonucleotide FF2 (Supplementary Figure S2A, Sigma Aldrich) and FF4 (Supplementary Figure S2A, Sigma Aldrich) were radiolabelled as indicated in (42) Protein complexes were prepared as indicated before then mixed with radiolabelled substrates (10 nM) with UPF1-HD (50 nM) with or without Np proteins in a buffer containing 20 mM MES pH 6.5, 150 mM potassium acetate, 2 mM DTT, 0.2 μg/μL BSA and 6% (v/v) glycerol. The samples were incubated at 30°C for 20 min before being resolved by native 6.5% polyacrylamide (19:1) gel electrophoresis and analyzed by phosphorimaging.

Results

Nucleocapsid protein of SARS-CoV-2 directly interacts with UPF1

Several lines of evidences indicated that Np from different CoVs is associated to cellular NMD inhibition via interaction with UPF1-containing RNP (19,36,37,39). Indeed, Np is associated with the incoming viral RNA genome (gRNA) and could represent the first line of defense against cellular RNA decay factors. To investigate the potential interaction between SARS-CoV-2 Np and endogenous UPF1, we initially transfected HEK 293T cells with a plasmid expressing Strep-tagged Np. Following RNAse A treatment to eliminate RNA-bridged associations ((44) Supplementary Figure S1A), we performed co-immunoprecipitations directed against endogenous UPF1 (Figure 1A). The effective interaction between UPF1 and Np was visualized by western blot using Anti-UPF1 and Anti-Strep-tag antibodies, respectively (Figure 1A).

To further characterize the impact of Np on UPF1 activity, we performed an *in vitro* study of the SARS-CoV-2 Np-UPF1 interaction, using purified recombinant proteins and protein fragments. As in most nidoviruses, SARS-CoV-2 Np is composed of two structured domains: the N-terminal domain (Np-NTD) between amino acids [aa] 50 and 140 and the C-terminal domain (Np-CTD) between aa 250 and 370. Additionally, it contains two intrinsically disordered regions (IDRs) located at the N- and C-termini, as well as one Serine-Arginine (S/R) rich linker between the NTD and CTD (aa 140–250; Figure 1B). We used different truncations of Np: the Np-L (aa 50–370) depleted of the IDR extremities (Figure 1B); the Np-NTD (aa 40–140) and Np-CTD (aa 250–330; Figure 1B). Concerning UPF1 recombinant proteins, the boundaries

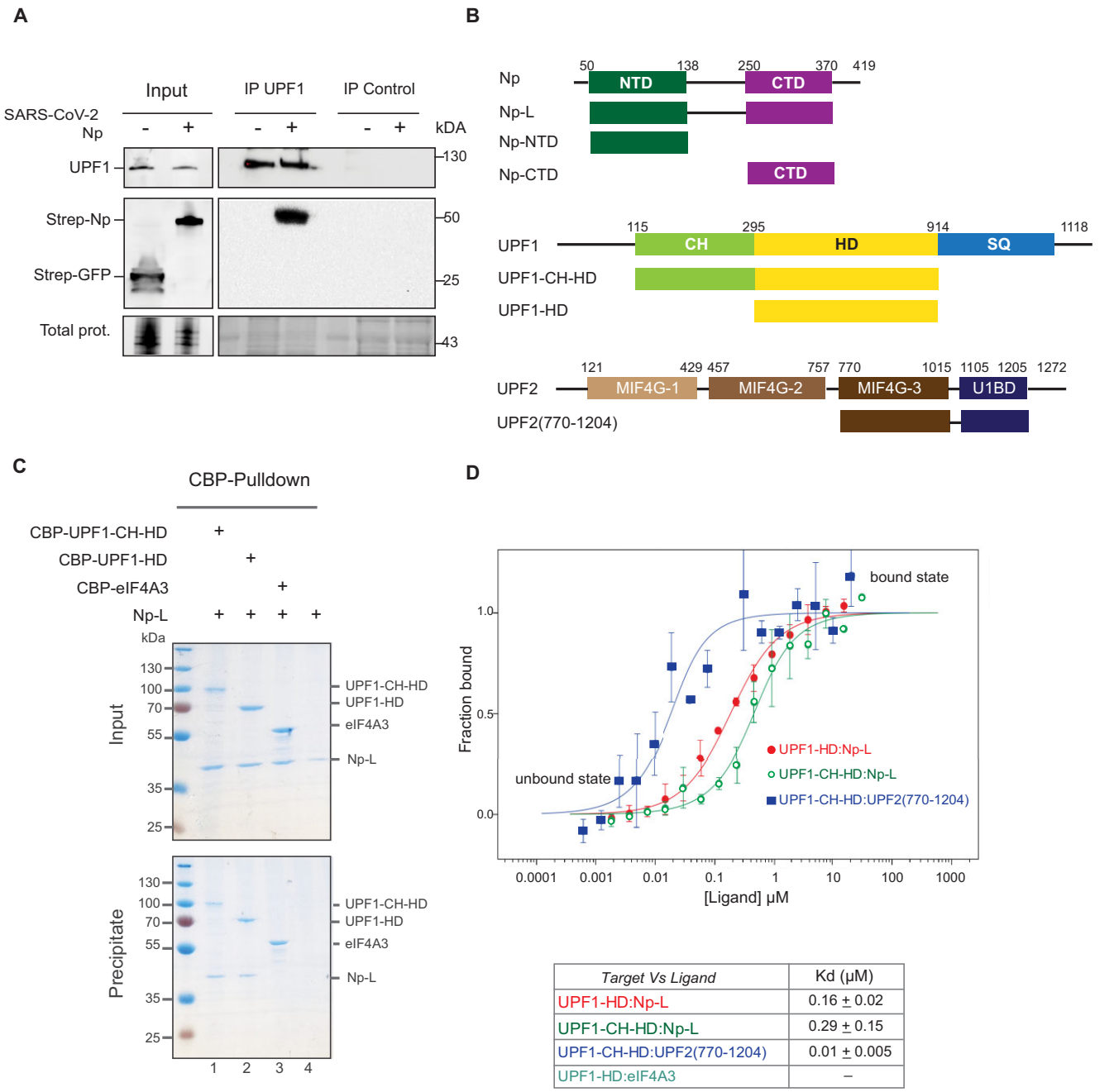

Target Vs Ligand	Kd (µM)
UPF1-HD:Np-L	0.16 ± 0.02
UPF1-CH-HD:Np-L	0.29 ± 0.15
UPF1-CH-HD:UPF2(770-1204)	0.01 ± 0.005
UPF1-HD:eIF4A3	–

Figure 1. SARS-CoV-2 Np directly interacts with UPF1 in cellulo and *in vitro*. (**A**) Co-immunuprecipitation of endogenous UPF1 with SARS-CoV-2 Np in HEK 293T cells. Western blot of UPF1 and strep-tagged SARS-CoV-2 Np before (input, left panel) and after immunoprecipitation (right panel) of endogenous UPF1. As a negative control, immunoprecipitation was also performed using a control serum. (**B**) Schematic diagram showing the SARS-CoV-2 Np, UPF1 and UPF2 domains used for this study. Structural domains are represented by rectangles and (predicted/confirmed) flexible regions by black lines. (**C**) Pulldown experiment using CBP-UPF1-CH-HD (lane 1), CBP-UPF1-HD (lane 2) or CBP-eIF4A3 (lane 3) as bait. After incubation, protein mixtures before (input 20% of total) or after precipitation (precipitate) were separated on a 12% SDS-PAGE gel and visualized by Coomassie staining. (**D**) MST quantification of UPF1 (target) –Np (ligand) interaction. The graph depicts the titration of Np-L or UPF2(770–1204) to a constant amount of UPF1-HD or UPF1-CH-HD fluorescently labeled. The binding curve represents the ligand concentration in a logarithmic scale, versus the proportion of the target that is bound by the ligand (fraction bound). The binding curve was fitted using a non-linear regression model to calculate the dissociation constant (KD). Filled dots and empty dots are UPF1-HD and UPF1-CH-HD versus Np-L, respectively; triangles are UPF1-CH-HD versus UPF2(770–1204). Data points represent the mean values obtained from three independent experiments, with error bars indicating the standard deviation. At the bottom, the KD values from MST experiments are summarized.

between its three domains were defined according to previous structural and biochemical studies (41,45). We produced UPF1 containing the helicase domain (UPF1-HD aa 295–914) and a protein containing both, the HD and the N-terminal (CH) domain (UPF1-CH-HD; aa 115–914; Figure 1B), and a DEAD box helicase eIF4A3 as a control.

CBP and/or N- or C-terminal His-tagged proteins were purified as described in methods section. To assess the direct interaction of UPF1 and Np, we incubated the two different UPF1 fragments with Np-L and performed CBP pull-down (Figure 1C). After extensive washes, input and eluted protein(s) were fractionated by SDS-PAGE and visualized by Coomassie staining. Np-L were co-precipitated when CBP-UPF1-CH-HD or CBP-UPF1-HD were used as bait (Figure 1C, lanes 1 and 2) and compared to CBP-eIF4A3 (Figure 1C, lane 3). Furthermore, MST confirmed these interactions and determined a KD of 160 nM for UPF1-HD:Np-L and 290 nM UPF1-CH-HD:Np-L (Figure 1D and Supplementary Figure S1B). The MST assay using only Np fragments indicated that the Np-CTD domain interacts more effectively with UPF1-HD than the Np-NTD (Supplementary Figure S1B). As a control, we also used the UPF2 fragment containing the UPF1-binding region (aa 770–1204; Figure 1B) and found an expected very high affinity with UPF1-CH-HD resulting in a KD of 10 nM (Figure 1D and Supplementary Figure S1B). Altogether, these results demonstrate the direct interaction of SARS-CoV-2 Np and UPF1.

Np inhibits the unwinding activity of UPF1 and stabilizesan NMD-prone RNA substrate

UPF1 utilizes the energy derived from ATP hydrolysis to translocate on DNA or RNA substrates in a 5′-3′ direction. This translocation enables UPF1 to unwind NA duplexes or displace proteins located on the substrate (41,43,45). To assess whether SARS-CoV-2 Np impacts UPF1 activity, we initially monitored the enzyme's ability to unwind a DNA duplex. We chose DNA because it has been observed that the unphosphorylated Np forms biomolecular condensates in the presence of RNA (46–53). The DNA substrate was composed of a 12-nucleotide (nt) 5′ single-stranded DNA (ssDNA) followed by a 21-base-pair (bp) double-stranded DNA (dsDNA) region (Figure 2A upper scheme and Supplementary Figure S2A). The substrate was first incubated with UPF1-HD, which exclusively binds to the ssDNA portion. Subsequently, the unwinding reaction was triggered by ATP addition, and the unwinding reaction was monitored under a pre-steady state regimen (see 'Materials and methods') by tracking the radiolabeled bottom-strand DNA oligonucleotide (Figure 2A; (41,42)). Under these conditions, only the first round of unwinding was monitored during the reaction (single-run conditions). Unwinding efficiencies were determined based on the proportions of 32P-labeled ssDNA accumulated over time (Figure 2A and B).

Remarkably, the unwinding activity of UPF1-HD is strongly affected by the presence of the Np-L protein (Figure 2A and B). Indeed, the amplitude of the reaction with UPF1-HD:Np-L is reduced by approximately 6-fold when compared to that obtained with Upf1-HD alone (Figure 2B). In contrast, the inhibition of the UPF1-HD unwinding by the Np-NTD and Np-CTD truncations was reduced by half when compared to the Np-L (Figure 2A and B). These data clearly demonstrate that only the Np-L fully inhibits the helicase activity of UPF1 ant that N- and C-terminal domains of Np produce a significant but a lesser extent effect.

It is possible that this inhibition of UPF1 enzymatic activity may result in an inhibition of NMD, as already observed for MHV coronavirus (19). Thus we monitored these activities with an NMD assay performed in HeLa cells expressing SARS-CoV-2 Np. In this test, we first analyzed the level of mRNAs transcribed from transfected β-globin minigenes, WT (Gl-WT) or with a Gl-PTC. Both transcripts undergo splicing, and only the Gl-PTC reporter is targeted by NMD and degraded (Supplementary Figure S2B). When NMD is inhibited, the Gl-PTC mRNA is stabilized, leading to increased steady state levels. In contrast, Gl-WT stability is unaffected by NMD (Supplementary Figure S2B and Figure 2C). Our quantitative RT-qPCR analysis revealed that Gl-PTC transcript levels are significantly increased in the presence of Np compared to Gl-WT mRNA under the same conditions (Figure 2C). To further confirm this, we used the African Green monkey kidney cell line called Vero E6, a suitable model for studying SARS-CoV-2 replication. NMD activity, which had not been previously evaluated in Vero E6 cells, was successfully monitored after treatment with UPF1 siRNA or SMG1 kinase inhibitor (SMG1I – (54); Supplementary Figure S2C and S2D). We then measured the impact of SARS-CoV-2 Np overexpression (Figure 2D upper panel) on the Gl-PTC half-life, as described in previous studies (12,20), and found that Np can inhibit reporter NMD in Vero E6 (Figure 2D).

The Np physically inhibits the progression of UPF1 on the substrate

The physicochemical properties of SARS-CoV-2 Np allow for its non-specific binding to NAs, including both ssDNA and dsDNA, *in vitro* (55–58). This raises the issue that Np could affect UPF1 through an indirect mechanism, primarily acting on the NA substrate. To understand how Np affects UPF1's unwinding activity, we studied the enzymatic properties associated with its helicase. As mentioned, unwinding is fueled by ATP hydrolysis, so we investigated the effect of Np on this process. Indeed, the ATP hydrolysis activity of UPF1-HD is identical whether Np-L is present or not suggesting rather an indirect mechanism (Figure 3A).

Then, we focused on the nucleoprotein remodeling activity of UPF1. UPF1 is able to displace streptavidin bound to a biotinylated RNA substrate or ssDNA binding proteins coating the DNA by translocation (43,59). To measure this activity, we conducted a streptavidin displacement assay: briefly, UPF1-HD and Np-L were pre-incubated at 37°C then a radiolabeled substrate is added as indicated in Figure 3B (upper scheme), before the reaction was initiated by adding ATP, magnesium and an excess of biotin to trap free streptavidin molecules. Time-course aliquots were then analyzed on a native polyacrylamide gel to separate free DNA from streptavidin-bound DNAs (Figure 3B). Remarkably, both UPF1–HD and the UPF1–HD:Np-L complex efficiently displaced the streptavidin from the substrate indicating that the translocation ability of UPF1 is not affected by the presence of SARS-CoV-2 Np (Figure 3B left and right panels). An efficient streptavidin displacement was also observed using UPF1–HD:Np-NTD and UPF1–HD:Np-CTD protein complexes (Supplementary Figure S2E and S2F).

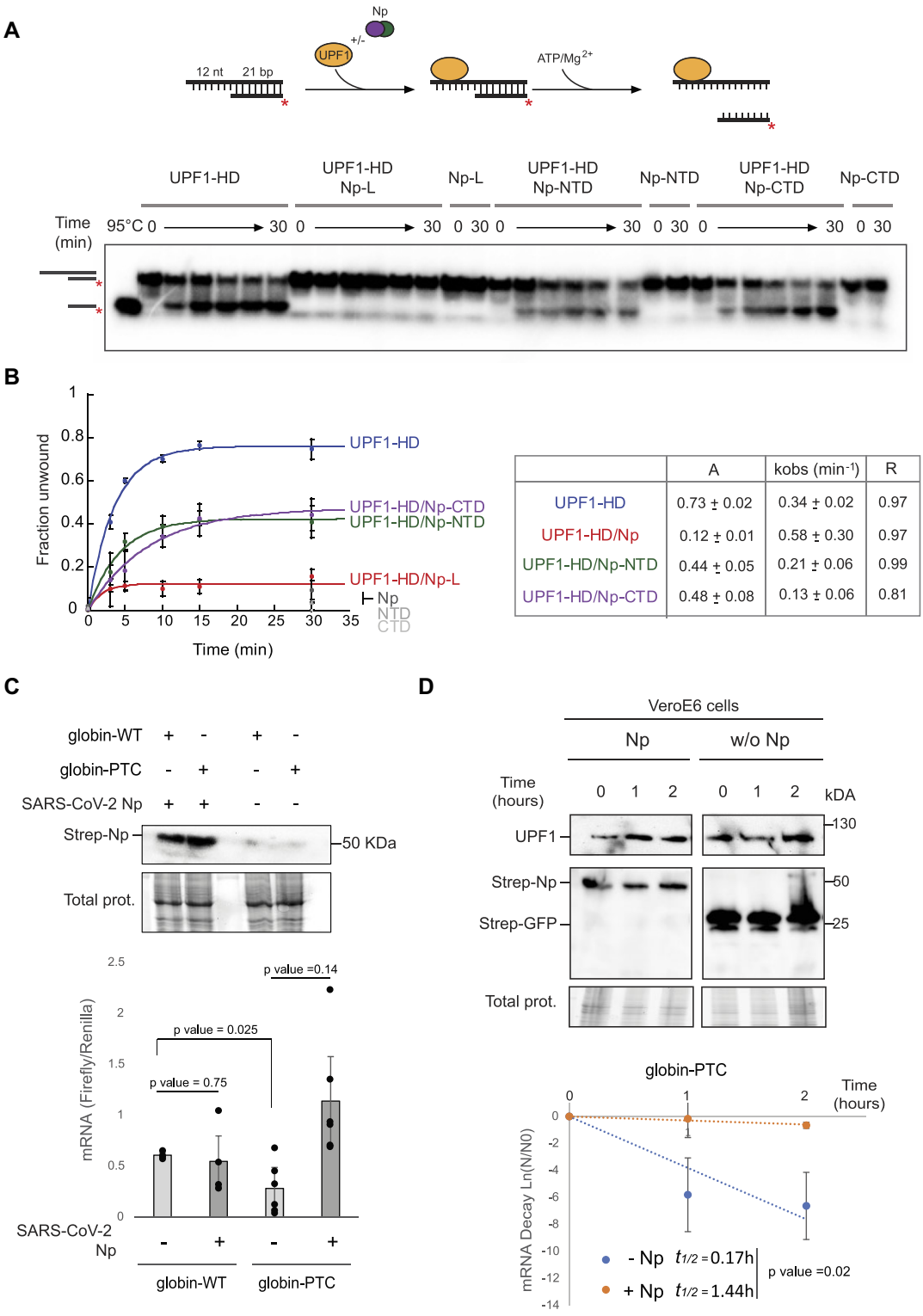

	A	kobs (min^{-1})	R
UPF1-HD	0.73 ± 0.02	0.34 ± 0.02	0.97
UPF1-HD/Np	0.12 ± 0.01	0.58 ± 0.30	0.97
UPF1-HD/Np-NTD	0.44 ± 0.05	0.21 ± 0.06	0.99
UPF1-HD/Np-CTD	0.48 ± 0.08	0.13 ± 0.06	0.81

Figure 2. SARS-CoV-2 Np inhibits UPF1 unwinding activity and cellular NMD. (**A**) A representative gel showing ATP-induced unwinding of the dsDNA substrate with 5′ overhangs of 12 nucleotides by UPF1-HD, the UPF1-HD:Np-L, UPF1-HD:Np-NTD and UPF1-HD:Np-CTD preformed complex, and Np-L, Np-NTD and Np-CTD alone. The substrate and the experimental workflow are depicted at the top of the gel. In the control lanes, ATP was replaced by ADPNP or samples were heat-denatured (95°C). (**B**) Graph showing the fraction of DNA oligonucleotide released over time. Data points derived from four independent experiments were fitted to the pseudo-first order equation y = A[1-e(-kt)], where A and k represent, respectively, the amplitude and the rate constant of the unwinding reaction. (**C**) NMD assay was performed in cells overexpressing or not the SARS-CoV-2 Np. In the upper panel, the western blot displays the overexpression levels of SARS-CoV-2 Np. NMD efficiency was assessed by the quantitative detection of NMD reporter mRNAs at steady state. Relative levels of GI-WT and GI-PTC mRNAs were determined by RT-qPCR. The statistical significance was supported by a T test with three independent biological replicates. (**D**) NMD assay was conducted in Vero E6 cells expressing SARS-CoV-2 Np or GFP as indicated. The half-life ($t_{\frac{1}{2}}$) of GI-PTC mRNA, which is sensitive to NMD, was evaluated under both conditions. Statistical significance was determined using a T-test based on three independent biological replicates.

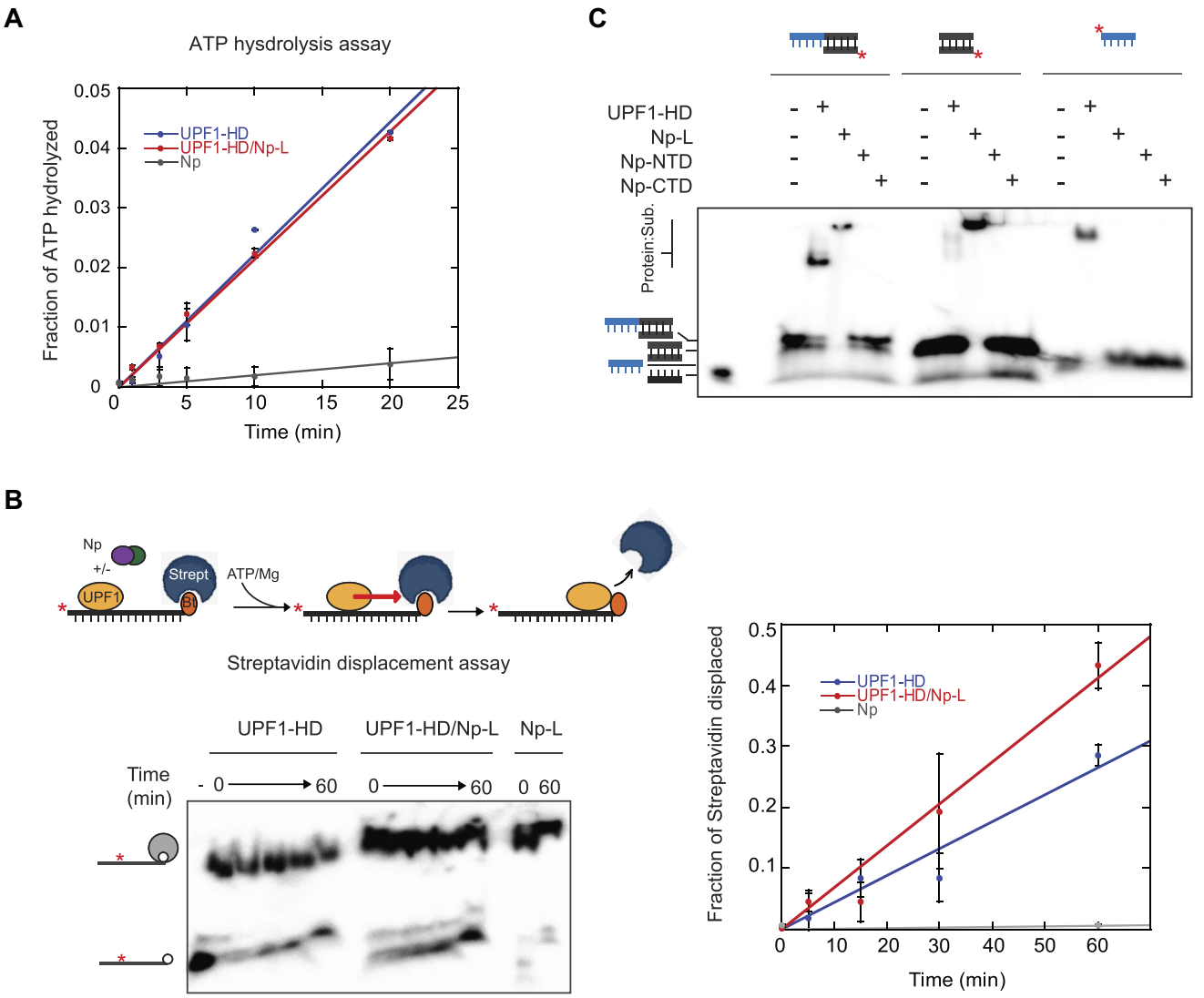

Figure 3. SARS-CoV-2 Np does not affect the ATPase and protein-displacement functions of UPF1. (**A**) Graph showing the percentage of ATP hydrolyzed as a function of time by the UPF1–HD, UPF1–HD:Np-L-preformed complex, and Np-L alone under conditions of steady-state ATPase turnover (see 'Materials and methods' section). (**B**) Time course of an active displacement of streptavidin from a 3′ biotinylated DNA by UPF1-HD, the UPF1-HD:Np-L preformed complex, and Np-L alone. The pipeline of the experiment is showed at the top of the gel. At various times (see Methods section) aliquots from the helicase reaction were mixed in a quench buffer and loaded immediately on 8% polyacrylamide gel containing 0.3% of SDS to selectively denature protein/s:DNA complexes without altering biotin–streptavidin interaction. On the right, graph showing the fraction of streptavidin displaced as a function of time (min). The bound product fraction at time 0 is calculated using Eq. F0 = P0/(R0 + P0) and the product fractions at time 't' using Eq. Ft=(Pt-F0(Pt + Rt))/((1-F0)(Pt + Rt)) where P is the intensity of the band corresponding to the reaction product (biotinylated DNA) and R the intensity of the substrate (biotinylated DNA bound to the streptavidin) in the corresponding gel. Data points (Mean ± SD) derived from three independent experiments. Data were fitted with KaleidaGraph (Synergy software) using a linear equation. (**C**) Representative native 6.5% polyacrylamide gels illustrating the interaction of UPF1-HD and Np-L, Np-NTD and Np-CTD proteins with different DNA substrates depicted at the top of the gel. The radiolabeled 5′ extremity is showed by a red star, the overhang DNA is in blue and the dsDNA in black. The substrates were incubated with the same concentrations of proteins used in helicase or streptavidin displacement assays.

One possible explanation for the inhibition of helicase activity without alteration of ATP hydrolysis or translocation is that Np physically binds to the DNA substrate downstream of UPF1 binding site, thereby obstructing the progression of the enzyme. To test this hypothesis, we conducted an electrophoretic mobility shift assay under the same conditions as the enzymatic tests, using isolated portions of the DNA duplex substrate (Supplementary Figure S2A and Figure 3C). We used the entire DNA duplex, the 12-nts 5′ ssDNA overhang and the blunt dsDNA region. Each radiolabeled substrate was incubated with the indicated protein truncations, at the same concentration and under the same conditions used for the enzymatic tests. Our observations revealed that while UPF1-HD interacted with ssDNA only as anticipated, Np-L interacted with the dsDNA region of the substrate in our conditions (Figure 3C). Neither the Np-NTD nor the Np-CTD protein fragments exhibited stable interactions with either ssDNA or dsDNA (Figure 3C). This outcome corroborated the hypothesis that SARS-CoV-2 Np hampers the unwinding activity of UPF1 by binding to the structured region of the substrate.

SARS-CoV-2 Np binds also with UPF2 decreasing its interaction with UPF1

The physical block provided by Np for UPF1 progression and unwinding supports a model in which Np protects the incoming SARS-CoV-2 genome by binding to both structured and linear portions of the viral RNA (50). This protection might safeguard the viral genome from UPF1, preventing its degradation by the NMD pathway, but does not clearly account for the effects observed on the NMD reporter RNA (Figure 2C and D).

This NMD inhibition mediated by Np should occur through a mechanism distinct from physical RNA protection. Thus we tested the hypothesis that the activation step of UPF1 enzymatic exerted by UPF2 during NMD could be affected by the direct interaction of Np to UPF1. We performed a steady-state CBP pulldown of UPF1-CH-HD, using high amount of UPF2(770–1204) fragment and SARS-CoV-2 Np-L (Figure 4A). As expected, UPF2(770–1204) or Np-L were co-precipitated when CBP-UPF1-CH-HD was used as bait (Figure 4A; lanes 1 and 2) whereas mostly Np-L was co-precipitated by UPF1-CH-HD when present together with UPF2(770–1204) in the reaction mixture (Figure 4A; lane3). This result was quite surprising, as the affinity measured for the UPF1-CH-HD:UPF2(770–1204) interaction is about 30 times higher than for the UPF1-CH-HD:Np-L (Figure 1D and Supplementary Figure S1B). Thus we performed a dose-dependent pulldown assay using increasing amount of UPF2(770–1204) and Np (Figure 4B). In these conditions, we observed that at high concentrations, Np starts to bind UPF1 despite the presence of UPF2 (Figure 4B lanes 3 and 4), while high concentrations of UPF2 prevent the binding of Np to UPF1 (Figure 4B lanes 6–8). These data are consistent with measured KDs, although this setup does not allow us to distinguish between complexes composed of UPF1:UPF2, UPF1:Np or of the three proteins.

Thus we examined the possibility that Np interacts also with UPF2. Surprisingly, using MST, we observed an interaction between UPF2(770–1204) and SARS-CoV-2 Np-L with an affinity comparable to that of UPF1-CH-HD and UPF2(770–1204) under these conditions (Figure 4C). However, we observed differences in the Kd values obtained when measuring the affinity of UPF1-CH-HD and UPF2(770–1204) depending on which protein is labeled for the experiment. These differences are likely attributable to the presence of the fluorophore attached to UPF2, which can cause steric hindrance and decrease its affinity for UPF1-CH-HD.

To validate these observations in a physiologically relevant context, we tested the ability of SARS-CoV-2 Np to affect the UPF1/UPF2 interaction. To this end, we performed a HA immunoprecipitation in HEK 293T cells following ectopic DNA transfection with Myc-UPF1 and HA-UPF2 plasmids in presence or absence of SARS-CoV-2 Np. Western blot analysis revealed that both Strep-Np and Myc-UPF1 were co-immunoprecipitated with UPF2, both with and without RNAse treatment (Figure 4D). Consistently with CBP pulldown (Figure 4A and B) and MST (Figure 4C) experiments, the expression of Np resulted in a decrease in UPF1 co-immunoprecipitated by UPF2, supporting the idea that in cells, Np can associate with UPF2 and affect its interaction with UPF1 (Figure 4D). High concentrations of UPF2 prevent the binding of Np to UPF1 *in vitro* (Figure 4B) suggesting that higher levels of UPF2 in the cell may rescue the NMD reforming UPF1/UPF2 complex. Therefore, we measured the decay rate of Gl-PTC in Vero E6 cells with different combinations of ectopic SARS-CoV-2 Np and HA-UPF2. We observed that Np expression inhibited NMD stabilizing Gl-PTC mRNA (Figures 2D and 4E) and that overexpression of UPF2 in same conditions partially restored NMD (Figure 4E).

In conclusion, it is possible that Np affects the activation of UPF1 by altering its interaction with UPF2.

SARS-CoV-2 replication is modulated by ectopic expression of NMD factors

Finally, to recapitulate NMD inhibition by Np in a more physiological context, we monitored NMD activity in Vero E6 cells infected with a replicative SARS-CoV-2 strain containing a NeonGreen reporter gene (Figure 5A). Prior to viral infection, cells were transfected with the globin reporter plasmids (Gl-WT, Gl-PTC, as described in the methods. SARS-CoV-2 infection was confirmed by NeonGreen expression, and the reporter mRNA was quantified (Figure 5B). In SARS-CoV-2-infected Vero E6 cells, the steady-state levels of Gl-WT were lower than those in mock-infected cells, likely due to virus-mediated global translational reshaping of host gene expression. Conversely, the steady-state levels of Gl-PTC were significantly higher in infected cells compared to the mock, suggesting that NMD activity was suppressed in SARS-CoV-2-infected cells. (Figure 5B).

Following these results, we ectopically expressed UPF1 and UPF2 in VeroE6 cells prior to viral challenge with a SARS-CoV-2 strain bearing a NeonGreen reporter (Figure 5A). Overexpression of UPF1 and UPF2 was confirmed by flow cytometry using an anti-HA antibody (Supplementary Figure S3). The extent of viral replication was then assessed at 18 h post-infection by flow cytometry, enabling us to quantify the percentage of infected cells. Data were normalized to the control condition of infected cells in the absence of UPF1 and UPF2 proteins, set to 1. This relatively early time point was chosen to minimize unwanted side effects that may be due to UPF1/2 overexpression on the cell. Unexpectedly, under these conditions, the replication of SARS-CoV-2 was enhanced, albeit slightly, by ectopic expression of UPF1 and in contrast, it was inhibited upon overexpression of UPF2 (Figure 5C). This suggests that UPF1 and UPF2 have pro- and anti-viral functions, respectively. Overall, these data suggest that UPF proteins modulate SARS-CoV-2 replication.

Discussion

In the study of the ongoing arms race between viruses and hosts, increasing evidence shows that NMD is indeed a genuine defense mechanism against several positive-strand RNA viruses. Here, we showed the direct interaction of SARS-CoV-2 Np with UPF1 and UPF2 and demonstrated its consequences on inhibiting the NMD process. We observed a complex multilevel mechanism of UPF1 enzymatic regulation exerted by Np. The first level of regulation is exerted against the unwinding activity of UPF1. Although its ATP hydrolysis and translocation/remodeling activities remain unaffected by Np, the unwinding is strongly inhibited.

To shed light on this surprising effect, we performed a combination of bulk enzymatic assays using DNA substrates. The choice of DNA was motivated by the fact that UPF1 is not specific to a single NA *in vitro* and acts in several RNA- and DNA-related pathways in the cell (reviewed in (60) and (61)).

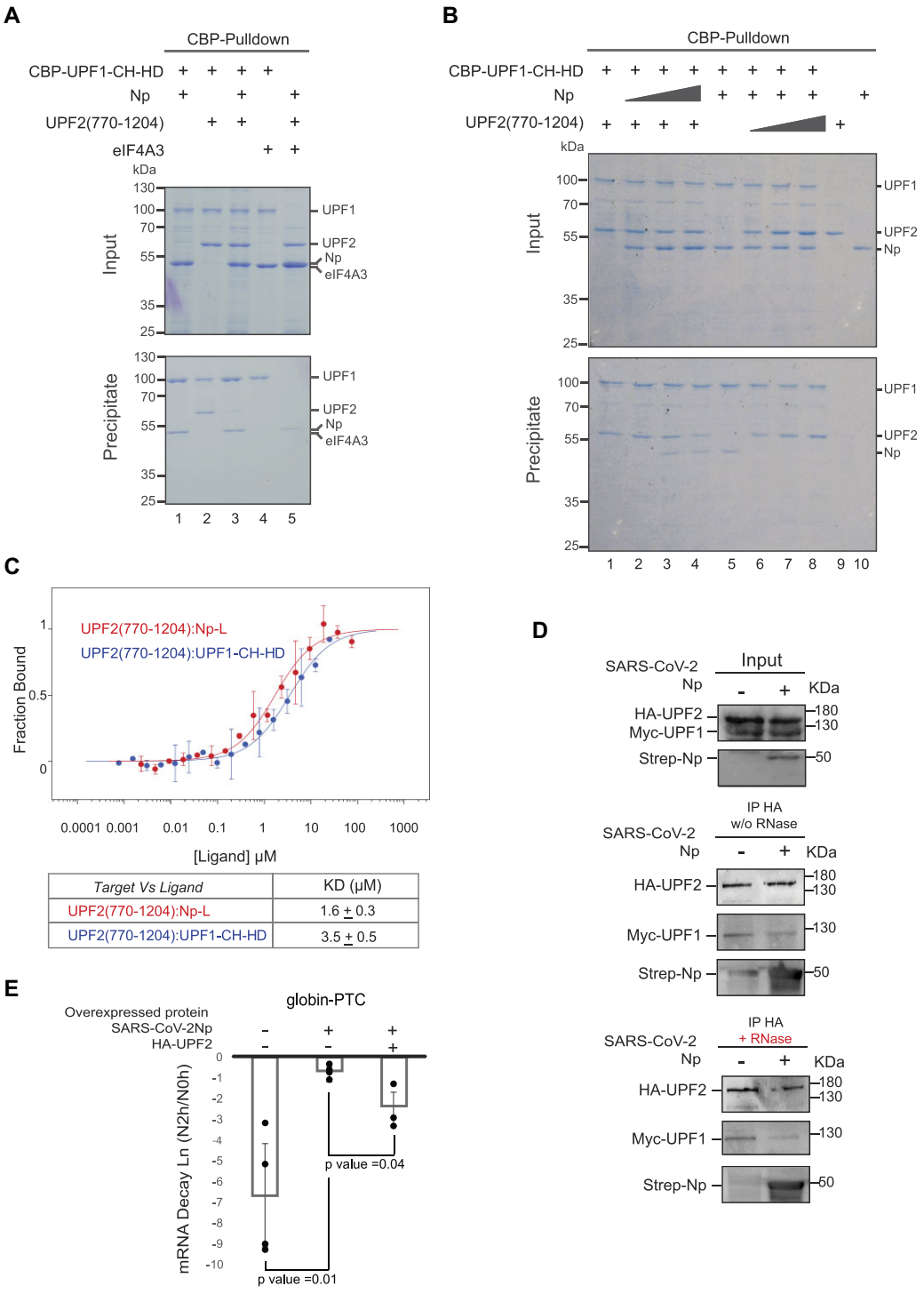

Figure 4. SARS-CoV-2 Np interacts with UPF1 and UPF2 affecting their interaction. (**A**) Pulldown experiment using CBP-UPF1-CH-HD (lanes 1 to 4) as bait and UPF2(770–1204), SARS-CoV-2 Np and eIF4A3 as preys. After incubation, protein mixtures before (input 20% of total) or after precipitation (precipitate) were separated on a 12% SDS-PAGE gel and visualized by coomassie staining. (**B**) Pulldown experiment using CBP-UPF1-CH-HD (lanes 1–8) as bait and UPF2(770–1204) (lane 1) and SARS-CoV-2 Np (lane 5) as preys. Three increasing amount of Np (lanes 2 to 4) or UPF2(770–1204) (lanes 6 to 8) were added to fixed amount of UPF1-UPF2 or UPF1-Np. (**C**) MST quantification of UPF2 (target) – Np or -UPF1 (ligands) interactions. The graph depicts the titration of Np-L or UPF1-CH-HD to a constant amount of UPF2(770–1204) fluorescently labeled. The binding curve represents the ligand concentration in a logarithmic scale, versus the proportion of the target that is bound by the ligand (fraction bound). The binding curve was fitted using a non-linear regression model to calculate the dissociation constant (KD). Red and blue curves are UPF2(770–1204) versus Np-L or UPF1-CH-HD respectively. Data points represent the mean values obtained from three independent experiments, with error bars indicating the standard deviation. At the bottom, the KD values from MST experiments are summarized. (**D**) HEK 293T cells were transfected with the indicated combinations of HA-UPF2, Myc-UPF1 and Strep-Np. Western blot analysis of UPF2, UPF1 and Np was performed both before (input) and after (IP HA) immunoprecipitation of HA-UPF2 and with (lower panel) or without RNase treatment (middle panel). (**E**) The NMD assay using the CI-PTC was performed in Vero E6 cells with the indicated combinations of SARS-CoV-2 Np and HA-UPF2. The data represent the mRNA level measured 2 h after triptolide treatment. Statistical significance was assessed using a T-test with three independent biological replicates.

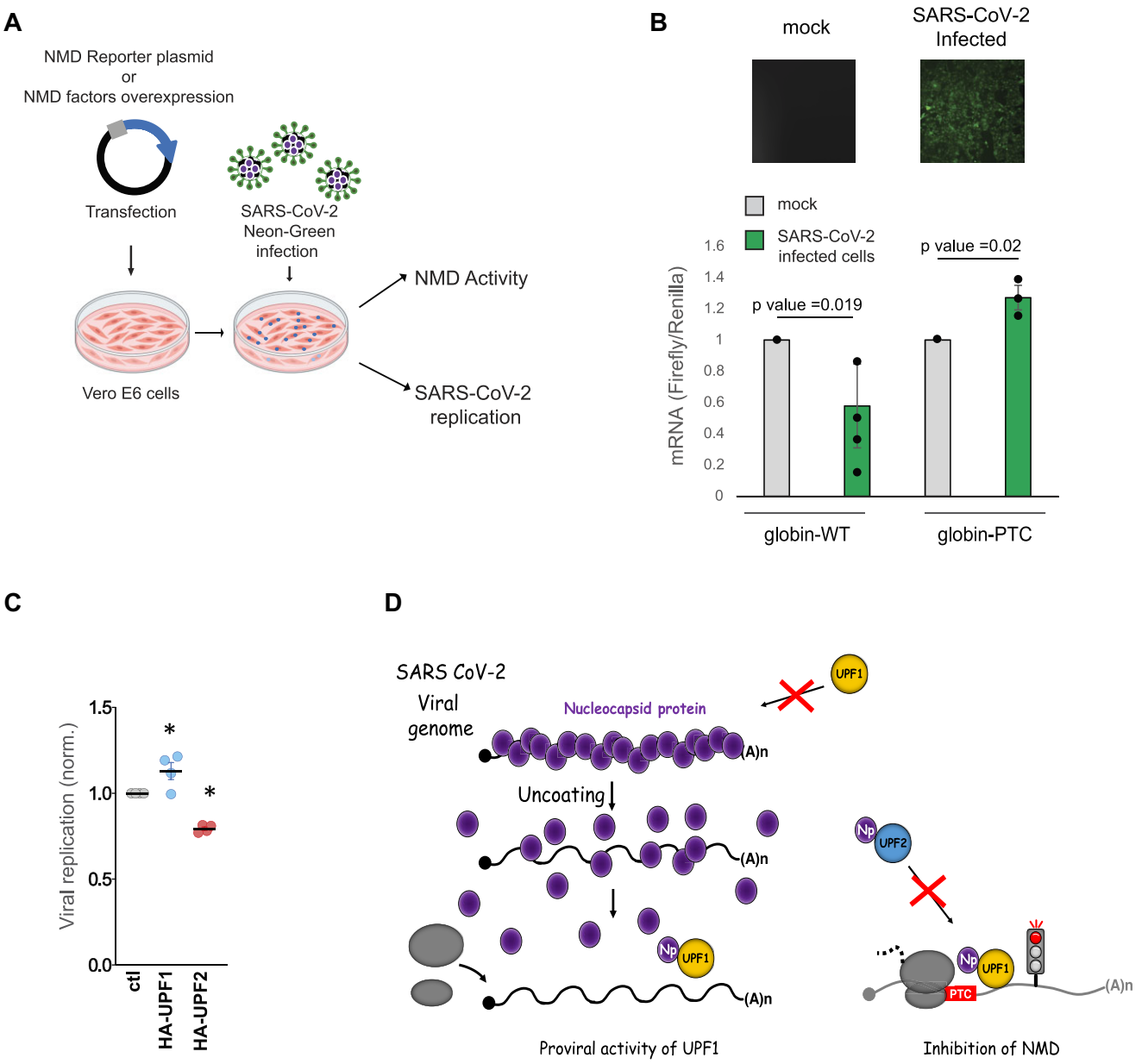

Figure 5. UPF1 and UPF2 have antagonistic effects on SARS-CoV-2 replication. (**A**) Schematic representation of the experiments performed with Vero E6 cells infected with a replicative strain of SARS-CoV-2. (**B**) An NMD assay was conducted on mock-infected or SARS-CoV-2-infected cells, as indicated by NeonGreen fluorescence expression (upper panel). Cl-WT and Gl-PTC mRNAs were quantified by qRT-PCR, and their relative levels were plotted in a graph. Statistical significance was determined using a T-test based on three independent biological replicates. (**C**) Vero E6 were transfected with DNA coding for HA-UPF1, HA-UPF2 or a control DNA. Twenty-eight hours later they were infected at a MOI of 0.1 with a Neon-Green bearing replicative-competent SARS-CoV-2 virus. The extent of viral replication and the overexpression of UPF1/ UPF2 were assessed 18 hours post-infection using flow cytometry. The graph presents averages and SEM from four independent experiments. * P value < 0.05, following an ordinary one-way Anova test between the indicated conditions. (**D**) Proposed mechanism of action. Upon entering the cell, the SARS CoV-2 genome is initially covered by Np shielding its genetic material from restriction factors and UPF1. Later, when Np detaches from the viral genome to allow access to the translation machinery, it binds to UPF1 and UPF2, altering their interaction and thereby inhibiting NMD. Given de modest proviral activity of UPF1, it is possible that the Np can hijack UPF1's functions to facilitate SARS-CoV-2 replication.

Moreover, the Np of SARS-CoV-2 has also been shown to promiscuously bind ss- and ds-NAs *in vitro* (55–58) but produces condensates only in the presence of ss- or dsRNA, which could bias the enzymatic study (46–53,62).

Using this DNA setup, we observed that UPF1 unwinding inhibition primarily occurs through the physical binding of Np to the double-stranded portion of the DNA substrate, thereby impeding the progression of UPF1. Even though Np has been shown to bind ssDNA in single-molecule studies (55), under our conditions, Np does not. However, the preference of Np for ssRNA sites flanked by stable stem-loops has been described (50,62), suggesting that Np could bind ssDNA when followed by a double-stranded region. Interestingly, until now, neither the presence of an avid ssDNA binder, such as Gp32-B, nor the presence of a biotin/streptavidin complex on ssRNA or ssDNA substrates has been able to impede the enzyme's progression (43). Notably, this loss of UPF1 accessibility to double-stranded substrate is consistent with the idea that Np, by tightly condensing the viral genome, serves as the first line of defense against cellular restriction factors.

The second level of regulation involves the direct interaction of SARS-CoV-2 Np with UPF1. This finding aligns with a proteomic study that identified the Np of SARS-CoV-2 as a UPF1 interactor (37), as well as with previous studies on other coronaviruses, where Np has been shown to inhibit NMD by interacting with UPF1-containing RNP complexes (19,36). In our experiments, Np binds to both UPF1 and UPF2 with micromolar or sub-micromolar dissociation constants (Kd), indicating a strong binding affinity (our work and Mallick et al.2024). This interaction decreases UPF1 and UPF2 binding: an essential step for the progression of NMD and RNA decay.

In this work, we also showed that UPF1 overexpression in SARS-CoV-2 infected cells slightly increased viral replication, while overexpression of UPF2 decreased it. First, the observation that an increased expression of UPF2 can inhibit viral replication supports the hypothesis that SARS-CoV-2 is sensitive to NMD and in turn, inhibits this process. Second, the finding that UPF1 overexpression increases it, is at first sight at odd with this hypothesis. At present, the reasons for this are unclear and it remains possible that despite the fact that they interact with each other, UPF1 and UPF2 may also play distinct additional roles in RNA metabolism. In support of this hypothesis, UPF1 overexpression enhanced viral RNA stability and translation of HIV-1, thereby promoting the production of viral proteins and the assembly of new virions (15,32,33), while UPF2 inhibits HIV-1 viral protein expression by promoting viral RNA decay (4,5,34,53).

In summary, our study elucidates a multifaceted strategy employed by SARS-CoV-2 to alter UPF1 functioning. By directly interacting with UPF1 and UPF2, the Np protein not only inhibits the helicase activity of UPF1 but also decreases the UPF1–UPF2 interaction and usurps UPF1 for the advantage of viral replication (Figure 5). This mechanism likely enhances the stability of viral RNAs, contributing to efficient viral replication. These findings highlight the importance of UPF1 and UPF2 in SARS-CoV-2 replication and suggest potential therapeutic targets within the NMD pathway to combat SARS-CoV-2 infection. Further research is needed to fully understand the broader implications of these interactions and to explore potential interventions that could disrupt the virus's ability to manipulate host RNA decay pathways.

Data availability

Any additional information required to reanalyze the data reported in this paper is available from the lead contact upon request.

Supplementary data

Supplementary Data are available at NAR Online.

Acknowledgements

We thank Dr. Christine Roden from the University of North Carolina at Chapel Hill, USA, for kindly providing us with the expression plasmid for SARS-CoV-2 Np. We acknowledge the support of the Protein Science Facility (PSF) of SFR Biosciences (UAR3444/CNRS, US8/Inserm, ENS de Lyon, UCBL), especially Virginie Gueguen-Chaignon and Céline Freton for their assistance, and Frédéric Galisson for his help with radioactive sources..

Author contributions: V.M., A.C. and F.F. conceptualized the study and conceived and designed experiments. V.N., F.G.B., C.R. and P.D.C. acquired and analyzed the majority of the *in vitro* biochemical experiments. M.M.H., S.D. and A.R. performed cellular and viral experiments. F.F. wrote the manuscript and all other authors edited it.

Funding

Fondation Innovations en Infectiologie [FINOVI 247 479 to V.M., A.C. and F.F.]; National Center for Scientific Research - CNRS; ANRS- Emerging infectious diseases [ECTZ245897 to F.F.]; French National Research Agency [ANR-24-CE15-2986-03 to F.F. and A.C.].

Conflict of interest statement

None declared.

References

1. Chang,J.C., Temple,G.F., Trecartin,R.F. and Kan,Y.W. (1979) Suppression of the nonsense mutation in homozygous beta 0 thalassaemia. *Nature*, **281**, 602–603.
2. Maquat,L.E., Kinniburgh,A.J., Rachmilewitz,E.A. and Ross,J. (1981) Unstable beta-globin mRNA in mRNA-deficient beta o thalassemia. *Cell*, **27**, 543–553.
3. Losson,R. and Lacroute,F. (1979) Interference of nonsense mutations with eukaryotic messenger RNA stability. *Proc. Nat. Acad. Sci. USA*, **76**, 5134–5137.
4. Mendell,J.T., Sharifi,N.A., Meyers,J.L., Martinez-Murillo,F. and Dietz,H.C. (2004) Nonsense surveillance regulates expression of diverse classes of mammalian transcripts and mutes genomic noise. *Nat. Genet.*, **36**, 1073–1078.
5. Kurosaki,T., Popp,M.W. and Maquat,L.E. (2019) Quality and quantity control of gene expression by nonsense-mediated mRNA decay. *Nat. Rev. Mol. Cell Biol.*, **20**, 406–420.
6. Ahmed,M.R. and Du,Z. (2023) Molecular interaction of nonsense-mediated mRNA decay with viruses. *Viruses*, **15**, 816.
7. Popp,M.W., Cho,H. and Maquat,L.E. (2020) Viral subversion of nonsense-mediated mRNA decay. *RNA*, **26**, 1509–1518.
8. Mocquet,V., Durand,S. and Jalinot,P. (2015) How retroviruses escape the nonsense-mediated mRNA decay. *AIDS Res. Hum. Retroviruses*, **31**, 948–958.

9. Weil,J.E. and Beemon,K.L. (2006) A 3′ UTR sequence stabilizes termination codons in the unspliced RNA of Rous sarcoma virus. *RNA*, **12**, 102–110.
10. Napthine,S., Yek,C., Powell,M.L., Brown,T.D. and Brierley,I. (2012) Characterization of the stop codon readthrough signal of Colorado tick fever virus segment 9 RNA. *RNA*, **18**, 241–252.
11. Quek,B.L. and Beemon,K. (2014) Retroviral strategy to stabilize viral RNA. *Curr. Opin. Microbiol.*, **18**, 78–82.
12. Mocquet,V., Neusiedler,J., Rende,F., Cluet,D., Robin,J.P., Terme,J.M., Duc Dodon,M., Wittmann,J., Morris,C., Le Hir,H., *et al.* (2012) The human T-lymphotropic virus type 1 tax protein inhibits nonsense-mediated mRNA decay by interacting with INT6/EIF3E and UPF1. *J. Virol.*, **86**, 7530–7543.
13. Garcia,D., Garcia,S. and Voinnet,O. (2014) Nonsense-mediated decay serves as a general viral restriction mechanism in plants. *Cell Host Microbe*, **16**, 391–402.
14. Balistreri,G., Horvath,P., Schweingruber,C., Zund,D., McInerney,G., Merits,A., Muhlemann,O., Azzalin,C. and Helenius,A. (2014) The host nonsense-mediated mRNA decay pathway restricts Mammalian RNA virus replication. *Cell Host Microbe*, **16**, 403–411.
15. Ajamian,L., Abel,K., Rao,S., Vyboh,K., Garcia-de-Gracia,F., Soto-Rifo,R., Kulozik,A.E., Gehring,N.H. and Mouland,A.J. (2015) HIV-1 recruits UPF1 but excludes UPF2 to promote nucleocytoplasmic export of the genomic RNA. *Biomolecules*, **5**, 2808–2839.
16. Toro-Ascuy,D., Rojas-Araya,B., Valiente-Echeverria,F. and Soto-Rifo,R. (2016) Interactions between the HIV-1 unspliced mRNA and host mRNA decay machineries. *Viruses*, **8**, 320.
17. Tang,X., Zhu,Y., Baker,S.L., Bowler,M.W., Chen,B.J., Chen,C., Hogg,J.R., Goff,S.P. and Song,H. (2016) Structural basis of suppression of host translation termination by Moloney Murine Leukemia Virus. *Nat. Commun.*, **7**, 12070.
18. Fontaine,K.A., Leon,K.E., Khalid,M.M., Tomar,S., Jimenez-Morales,D., Dunlap,M., Kaye,J.A., Shah,P.S., Finkbeiner,S., Krogan,N.J., *et al.* (2018) The cellular NMD pathway restricts Zika Virus infection and is targeted by the viral capsid protein. *mBio*, **9**, e02126-18.
19. Wada,M., Lokugamage,K.G., Nakagawa,K., Narayanan,K. and Makino,S. (2018) Interplay between coronavirus, a cytoplasmic RNA virus, and nonsense-mediated mRNA decay pathway. *Proc. Nat. Acad. Sci. USA*, **115**, E10157–E10166.
20. Fiorini,F., Robin,J.P., Kanaan,J., Borowiak,M., Croquette,V., Le Hir,H., Jalinot,P. and Mocquet,V. (2018) HTLV-1 tax plugs and freezes UPF1 helicase leading to nonsense-mediated mRNA decay inhibition. *Nat. Commun.*, **9**, 431.
21. Ramage,H.R., Kumar,G.R., Verschueren,E., Johnson,J.R., Von Dollen,J., Johnson,T., Newton,B., Shah,P., Horner,J., Krogan,N.J., *et al.* (2015) A combined proteomics/genomics approach links hepatitis C virus infection with nonsense-mediated mRNA decay. *Mol. Cell*, **57**, 329–340.
22. Li,M., Johnson,J.R., Truong,B., Kim,G., Weinbren,N., Dittmar,M., Shah,P.S., Von Dollen,J., Newton,B.W., Jang,G.M., *et al.* (2019) Identification of antiviral roles for the exon-junction complex and nonsense-mediated decay in flaviviral infection. *Nat. Microbiol.*, **4**, 985–995.
23. May,J.P., Yuan,X., Sawicki,E. and Simon,A.E. (2018) RNA virus evasion of nonsense-mediated decay. *PLoS Pathog.*, **14**, e1007459.
24. Contu,L., Balistreri,G., Domanski,M., Uldry,A.C. and Muhlemann,O. (2021) Characterisation of the Semliki Forest Virus-host cell interactome reveals the viral capsid protein as an inhibitor of nonsense-mediated mRNA decay. *PLoS Pathog.*, **17**, e1009603.
25. Sarkar,R., Banerjee,S., Mukherjee,A. and Chawla-Sarkar,M. (2022) Rotaviral nonstructural protein 5 (NSP5) promotes proteasomal degradation of up-frameshift protein 1 (UPF1), a principal mediator of nonsense-mediated mRNA decay (NMD) pathway, to facilitate infection. *Cell Signal.*, **89**, 110180.
26. Nakano,K., Karasawa,N., Hashizume,M., Tanaka,Y., Ohsugi,T., Uchimaru,K. and Watanabe,T. (2022) Elucidation of the mechanism of host NMD suppression by HTLV-1 Rex: dissection of Rex to identify the NMD inhibitory domain. *Viruses*, **14**, 344.
27. Xu,P., Tong,W., Kuo,C.Y., Chen,H.H. and Wang,R.Y.L. (2023) The Upf1 protein restricts EV-A71 viral replication. *Microbes Infect.*, **25**, 105220.
28. Hogg,J.R. (2016) Viral evasion and manipulation of host RNA quality control pathways. *J. Virol.*, **90**, 7010–7018.
29. May,J.P., Johnson,P.Z., Ilyas,M., Gao,F. and Simon,A.E. (2020) The multifunctional long-distance movement protein of pea enation mosaic Virus 2 protects viral and host transcripts from nonsense-mediated decay. *mBio*, **11**, e00204-20.
30. Baker,S.L. and Hogg,J.R. (2017) A system for coordinated analysis of translational readthrough and nonsense-mediated mRNA decay. *PLoS One*, **12**, e0173980.
31. Nakano,K. and Watanabe,T. (2016) HTLV-1 rex tunes the cellular environment favorable for viral replication. *Viruses*, **8**, 58.
32. Ajamian,L., Abrahamyan,L., Milev,M., Ivanov,P.V., Kulozik,A.E., Gehring,N.H. and Mouland,A.J. (2008) Unexpected roles for UPF1 in HIV-1 RNA metabolism and translation. *RNA*, **14**, 914–927.
33. Serquina,A.K., Das,S.R., Popova,E., Ojelabi,O.A., Roy,C.K. and Gottlinger,H.G. (2013) UPF1 is crucial for the infectivity of human immunodeficiency virus type 1 progeny virions. *J. Virol.*, **87**, 8853–8861.
34. Rao,S., Amorim,R., Niu,M., Temzi,A. and Mouland,A.J. (2018) The RNA surveillance proteins UPF1, UPF2 and SMG6 affect HIV-1 reactivation at a post-transcriptional level. *Retrovirology*, **15**, 42.
35. Fischer,F., Peng,D., Hingley,S.T., Weiss,S.R. and Masters,P.S. (1997) The internal open reading frame within the nucleocapsid gene of Mouse Hepatitis Virus encodes a structural protein that is not essential for viral replication. *J. Virol.*, **71**, 996–1003.
36. Emmott,E., Munday,D., Bickerton,E., Britton,P., Rodgers,M.A., Whitehouse,A., Zhou,E.M. and Hiscox,J.A. (2013) The cellular interactome of the coronavirus infectious bronchitis virus nucleocapsid protein and functional implications for virus biology. *J. Virol.*, **87**, 9486–9500.
37. Gordon,D.E., Jang,G.M., Bouhaddou,M., Xu,J., Obernier,K., White,K.M., O'Meara,M.J., Rezelj,V.V., Guo,J.Z., Swaney,D.L., *et al.* (2020) A SARS-CoV-2 protein interaction map reveals targets for drug repurposing. *Nature*, **583**, 459–468.
38. Schmidt,N., Lareau,C.A., Keshishian,H., Ganskih,S., Schneider,C., Hennig,T., Melanson,R., Werner,S., Wei,Y., Zimmer,M., *et al.* (2021) The SARS-CoV-2 RNA-protein interactome in infected human cells. *Nat. Microbiol.*, **6**, 339–353.
39. Lee,S., Lee,Y.S., Choi,Y., Son,A., Park,Y., Lee,K.M., Kim,J., Kim,J.S. and Kim,V.N. (2021) The SARS-CoV-2 RNA interactome. *Mol. Cell*, **81**, 2838–2850.
40. Xie,X., Muruato,A., Lokugamage,K.G., Narayanan,K., Zhang,X., Zou,J., Liu,J., Schindewolf,C., Bopp,N.E., Aguilar,P.V., *et al.* (2020) An infectious cDNA clone of SARS-CoV-2. *Cell Host Microbe*, **27**, 841–848.
41. Fiorini,F., Boudvillain,M. and Le Hir,H. (2013) Tight intramolecular regulation of the human Upf1 helicase by its N- and C-terminal domains. *Nucleic Acids Res.*, **41**, 2404–2415.
42. Fiorini,F., Bonneau,F. and Le Hir,H. (2012) Biochemical characterization of the RNA helicase UPF1 involved in nonsense-mediated mRNA decay. *Methods Enzymol.*, **511**, 255–274.
43. Fiorini,F., Bagchi,D., Le Hir,H. and Croquette,V. (2015) Human Upf1 is a highly processive RNA helicase and translocase with RNP remodelling activities. *Nat. Commun.*, **6**, 7581.
44. Morris,C., Wittmann,J., Jack,H.M. and Jalinot,P. (2007) Human INT6/eIF3e is required for nonsense-mediated mRNA decay. *EMBO Rep.*, **8**, 596–602.
45. Chakrabarti,S., Jayachandran,U., Bonneau,F., Fiorini,F., Basquin,C., Domcke,S., Le Hir,H. and Conti,E. (2011) Molecular

mechanisms for the RNA-dependent ATPase activity of Upf1 and its regulation by Upf2. *Mol. Cell*, **41**, 693–703.
46. Carlson,C.R., Asfaha,J.B., Ghent,C.M., Howard,C.J., Hartooni,N., Safari,M., Frankel,A.D. and Morgan,D.O. (2020) Phosphoregulation of PhaseSeparation by the SARS-CoV-2 N Protein Suggests a Biophysical Basis for its Dual Functions. *Mol. Cell*, **80**, 1092–1103.
47. Savastano,A., Ibanez de Opakua,A., Rankovic,M. and Zweckstetter,M. (2020) Nucleocapsid protein of SARS-CoV-2 phase separates into RNA-rich polymerase-containing condensates. *Nat. Commun.*, **11**, 6041.
48. Chen,H., Cui,Y., Han,X., Hu,W., Sun,M., Zhang,Y., Wang,P.H., Song,G., Chen,W. and Lou,J. (2020) Liquid-liquid phase separation by SARS-CoV-2 nucleocapsid protein and RNA. *Cell Res.*, **30**, 1143–1145.
49. Cubuk,J., Alston,J.J., Incicco,J.J., Singh,S., Stuchell-Brereton,M.D., Ward,M.D., Zimmerman,M.I., Vithani,N., Griffith,D., Wagoner,J.A., *et al.* (2020) The SARS-CoV-2 nucleocapsid protein is dynamic, disordered, and phase separates with RNA. *Nat. Commun.*, **12**, 1936.
50. Iserman,C., Roden,C.A., Boerneke,M.A., Sealfon,R.S.G., McLaughlin,G.A., Jungreis,I., Fritch,E.J., Hou,Y.J., Ekena,J., Weidmann,C.A., *et al.* (2020) Genomic RNA elements drive phase separation of the SARS-CoV-2 nucleocapsid. *Mol. Cell*, **80**, 1078–1091.
51. Jack,A., Ferro,L.S., Trnka,M.J., Wehri,E., Nadgir,A., Nguyenla,X., Fox,D., Costa,K., Stanley,S., Schaletzky,J., *et al.* (2021) SARS-CoV-2 nucleocapsid protein forms condensates with viral genomic RNA. *PLoS Biol.*, **19**, e3001425.
52. Lu,S., Ye,Q., Singh,D., Cao,Y., Diedrich,J.K., Yates,J.R. 3rd, Villa,E., Cleveland,D.W. and Corbett,K.D. (2020) The SARS-CoV-2 nucleocapsid phosphoprotein forms mutually exclusive condensates with RNA and the membrane-associated M protein. *Nat. Commun.*, **12**, 502.
53. Perdikari,T.M., Murthy,A.C., Ryan,V.H., Watters,S., Naik,M.T. and Fawzi,N.L. (2020) SARS-CoV-2 nucleocapsid protein phase-separates with RNA and with human hnRNPs. *EMBO J.*, **39**, e106478.
54. Gopalsamy,A., Bennett,E.M., Shi,M., Zhang,W.G., Bard,J. and Yu,K. (2012) Identification of pyrimidine derivatives as hSMG-1 inhibitors. *Bioorg. Med. Chem. Lett.*, **22**, 6636–6641.
55. Morse,M., Sefcikova,J., Rouzina,I., Beuning,P.J. and Williams,M.C. (2023) Structural domains of SARS-CoV-2 nucleocapsid protein coordinate to compact long nucleic acid substrates. *Nucleic Acids Res.*, **51**, 290–303.
56. Caruso,I.P., Dos Santos Almeida,V., do Amaral,M.J., de Andrade,G.C., de Araujo,G.R., de Araujo,T.S., de Azevedo,J.M., Barbosa,G.M., Bartkevihi,L., Bezerra,P.R., *et al.* (2022) Insights into the specificity for the interaction of the promiscuous SARS-CoV-2 nucleocapsid protein N-terminal domain with deoxyribonucleic acids. *Int. J. Biol. Macromol.*, **203**, 466–480.
57. Zeng,W., Liu,G., Ma,H., Zhao,D., Yang,Y., Liu,M., Mohammed,A., Zhao,C., Yang,Y., Xie,J., *et al.* (2020) Biochemical characterization of SARS-CoV-2 nucleocapsid protein. *Biochem. Biophys. Res. Commun.*, **527**, 618–623.
58. Zhou,R., Zeng,R., von Brunn,A. and Lei,J. (2020) Structural characterization of the C-terminal domain of SARS-CoV-2 nucleocapsid protein. *Mol. Biomed.*, **1**, 2.
59. Chapman,J.H., Craig,J.M., Wang,C.D., Gundlach,J.H., Neuman,K.C. and Hogg,J.R. (2022) UPF1 mutants with intact ATPase but deficient helicase activities promote efficient nonsense-mediated mRNA decay. *Nucleic Acids Res.*, **50**, 11876–11894.
60. Azzalin,C.M. and Lingner,J. (2006) The double life of UPF1 in RNA and DNA stability pathways. *Cell Cycle*, **5**, 1496–1498.
61. Kim,Y.K. and Maquat,L.E. (2019) UPFront and center in RNA decay: UPF1 in nonsense-mediated mRNA decay and beyond. *RNA*, **25**, 407–422.
62. Roden,C.A., Dai,Y., Giannetti,C.A., Seim,I., Lee,M., Sealfon,R., McLaughlin,G.A., Boerneke,M.A., Iserman,C., Wey,S.A., *et al.* (2022) Double-stranded RNA drives SARS-CoV-2 nucleocapsid protein to undergo phase separation at specific temperatures. *Nucleic Acids Res.*, **50**, 8168–8192.

Received: July 17, 2024. **Revised:** January 1, 2025. **Editorial Decision:** January 2, 2025. **Accepted:** January 6, 2025